Ocean Engineering 234 (2021) 109195

Contents lists available at ScienceDirect

Ocean Engineering

journal homepage: www.elsevier.com/locate/oceaneng

An evaluation of different RANS turbulence models for simulating breaking waves past a vertical cylinder

Sen Qu [a], Shengnan Liu [b,*], Muk Chen Ong [b]

[a] College of Shipbuilding Engineering, Harbin Engineering University, 150001, Harbin, China
[b] Department of Mechanical and Structural Engineering and Materials Science, University of Stavanger, 4036, Stavanger, Norway

ARTICLE INFO

Keywords:
Breaking wave
RANS
Turbulence models
Vertical cylinder
OpenFOAM

ABSTRACT

The purpose of the present study is to evaluate the performance of different turbulence models for predicting the interaction between breaking waves and a vertical cylinder based on the volume of fluid (VOF) method. Six different models are investigated in the present study, i.e., no turbulence model, the $k-\omega$ *SST* turbulence model, the buoyancy-modified $k-\omega$ *SST* turbulence model, the stabilized $k-\omega$ *SST* turbulence model, the modified stabilized $k-\omega$*SST* turbulence model and the realizable $k-\varepsilon$ turbulence model. The vertical cylinder is installed at the edge of a 1:10 slope on the bottom of the numerical wave tank. The numerical simulations are conducted by solving the unsteady Reynolds-Averaged Navier-Stokes (RANS) equations using waves2Foam (a solver based on the open-source Computational Fluid Dynamic (CFD) software OpenFOAM). The present numerical results of the surface elevations and the breaking wave forces are compared with published experimental data. The kinetic characteristics beneath the free surface including averaged velocity, turbulent kinetic energy and turbulent kinematic viscosity are also investigated. It is observed that the stabilized $k-\omega$ *SST* turbulence ($\lambda_2 = 0.05$, $\alpha_{\beta s} = 1.36$) and the buoyancy-modified $k-\omega$*SST* turbulence model ($\alpha_{\beta s} = 1.176$) effectively reduce the turbulent kinetic energy before wave breaking, but the predicted breaking wave forces on the cylinder are smaller than that of the experimental data. The $k-\omega$ *SST* turbulence model shows good agreement with the experimental data in terms of the free surface elevation and the breaking wave force, but it over-predicts the turbulent kinetic energy. The realizable $k-\varepsilon$ turbulence model does not give good predictions of both the free surface elevation and the breaking wave force as compared to the published experimental data.

1. Introduction

Breaking wave force is considered as one of the most complex events due to its strong nonlinear characteristics. It is still a challenging issue in terms of predicting breaking wave forces on marine structures. Circular cylinders are commonly used in the fields of coastal and offshore engineering as a basic structural component of wind turbines, offshore platforms and large floating structures. Therefore, it is important to accurately predict breaking wave forces on the cylinders for engineering design to ensure structural safety in extreme conditions.

Experiments play an important role to investigate the physics of breaking wave forces directly. Sawaragi and Nochino (1984) performed an experimental study of the breaking wave force on a vertical cylinder. They revealed that the front shape of the breaking wave determines the rising time of the impact force, and the magnitude of the force highly depends on the breaking pattern and the wave breaking point. Wienke et al. (2001) conducted a large-scale experiment to investigate the breaking wave loads acting on a vertical slender circular cylinder. They found that the breaking wave force based on the Morison equation is not sufficiently accurate. The impact force should be included in the equation, which considers the magnitude and duration of the impact. Irschik et al. (2005) performed an experiment of breaking waves past a vertical cylinder and an inclined cylinder which direction is parallel to the wave propagation. The breaking wave forces in different breaking points are studied. Moreover, Fast Fourier Transform (FFT) low-pass filter and Empirical Mode Decomposition (EMD) method were applied to divide the experimentally measured wave force into the quasi-static load and the dynamic part. They pointed out that the maximum wave force occurs when the wave breaks immediately in front of the cylinder.

In addition to the experimental investigations, Computational Fluid Dynamics (CFD) has become a good alternative tool. CFD can not only eliminate errors from human operations and experimental facilities, but also capture the details of various parameters reasonably well, such as velocity, acceleration and turbulent properties during the wave

* Corresponding author.
E-mail address: shengnan.liu@uis.no (S. Liu).

https://doi.org/10.1016/j.oceaneng.2021.109195
Received 19 June 2020; Received in revised form 10 May 2021; Accepted 17 May 2021
Available online 7 June 2021

breaking. Reynolds-Averaged Navier-Stokes (RANS) equations are widely used for investigating the breaking wave force on the structure in engineering applications due to the good performance in terms of the balance between numerical accuracy and efficiency. In recent decades, a large number of numerical simulations of the interaction between breaking waves and cylinders were conducted using RANS equations. Christensen et al. (2005) simulated the breaking wave past a vertical cylinder using the volume of fluid (VOF) method to study the wave run-up and breaking wave forces. They found that the peak value of the horizontal breaking wave force under a plunging breaker was much larger than that under a spilling breaker. Xiao and Huang (2014) employed the $k-\varepsilon$ turbulence model with the VOF method to investigate the breaking wave force on a vertical cylinder located at different positions along a slope in the surf zone. They found that the largest wave force occurred when the cylinder was located at 3/4 R (R is the maximum vertical run-up height) below the shoreline. Choi et al. (2015) used the VOF method to investigate breaking wave impact forces on a vertical cylinder and a inclined cylinder whose direction is parallel to the wave propagation. The effects of the vibration of the cylinders in the breaking wave forces in the experiment were studied. The computed breaking wave forces were in good agreement with the experimental data filtered by an FFT low pass filter and EMD. Bihs et al. (2016) studied the interaction between the breaking waves and a pair of cylinders placed in tandem using the $k-\omega$ turbulence model with the level set method (LSM). They found that the breaking wave forces acting on the cylinders were related to the location of breaking point and the distance between the cylinders. Kamath et al. (2016) and Chella et al. (2017) used the $k-\omega$ turbulence model with the LSM to study influences of breaking locations on the interactions of breaking waves and a vertical cylinder. The largest breaking wave force was observed when the overturning wave tongue was just below the wave crest level and impacted the cylinder. Subsequently, Chow et al. (2019) employed improved incompressible smoothed particle hydrodynamic (ISPH) method to simulate non-breaking and breaking waves past a vertical cylinder. The free surface elevation and steepness of the wave across the cylinder had a significant effect on the maximum loading on the structure. Local pressures on the cylinder near the free surface under breaking waves were higher than those of non-breaking waves. Liu et al. (2019) employed the $k-\omega SST$ turbulence model in combination with the VOF method to simulate the breaking wave past a vertical cylinder. It was observed that the breaking wave force on the cylinder was in a good agreement with the experimental measurement. Meanwhile, both slamming wave force and secondary load could generate the higher-harmonic wave force in the case of breaking wave.

Most of the above authors revealed that accurately predicting the wave breaking point is of great importance to obtain accurate breaking wave force on the cylinder. Lin and Liu (1998), Bradford (2000) and Xie (2013) applied RANS turbulence model ($k-\varepsilon$ and $k-\omega$) with VOF method to study the turbulence generation and dissipation of breaking waves in the surf zone. The turbulence levels in the wave crest before the wave break were significantly overestimated compared to the experimental data (Ting and Kirby, 1994). As a result, it led to an underprediction of the breaking wave height. Mayer and Madsen (2001) modified the production term of $k-\omega$ model using the vorticity of the mean flow instead of the local mean velocity gradient together with VOF method to simulate the spilling breaker. They eliminated the excessive generation of turbulent kinetic energy (TKE) outside the surf zone; and their numerical results were in good agreement with experimental measurements in term of elevation statistics. Brown et al. (2016) evaluated different RANS turbulence models with VOF method for predicting of spilling and plunging breakers in the surf zone. The realizable $k-\varepsilon$ model gave reasonable predictions of the surface elevation, time-averaged velocity and mean TKE profiles in terms of accuracy and numerical efficiency, while the $k-\omega$ SST turbulence model performed best for the wave elevation predictions. Devolder et al. (2018) proposed a buoyancy-modified $k-\omega$ turbulence model for breaking wave simulating. A buoyancy term is added in the turbulent kinetic energy equation, and is active before wave breaking to suppress the turbulence around the free surface. The density was explicitly included in the turbulence transport equations. It was pointed out that the buoyancy-modified turbulence models significantly reduced the common over-estimation of TKE around the free surface. Larsen and Fuhrman (2018) proposed a stabilized formulation for two-equation turbulence models using the addition of stress-limiting modification. The new model can avoid non-physical exponential growth of the turbulent kinetic energy and eddy viscosity in the nearly potential flow region. The numerical results of surface elevations can be predicted accurately. Meanwhile, reasonable turbulent kinetic energy and undertow velocity profiles were obtained. Liu et al. (2020) evaluated the performance of two free surface modelling approaches (continuous free surface conditions and free surface jump conditions) and three different $k-\omega$ SST turbulence models ($k-\omega$ SST , buoyancy-modified $k-\omega$ SST and free surface $k-\omega$ SST) for simulating spilling and plunging breakers, respectively. It was demonstrated that the free surface jump conditions eliminated spurious air velocity which can occur in the continuous free surface conditions due to imbalance between dynamic pressure gradient and density gradient. All the aforementioned research simulated wave breaking in the surf zone without considering the presence of structures. When the breaking wave impacts structures, the velocity of the wave crest front hitting the cylinder reduces to zero. A large wave impact force occurs on the cylinder. Meanwhile, the structure will also change the wave breaking point as compared to the case without structure. Therefore, it is necessary to evaluate the performance of different turbulence models on the interaction between breaking waves and structures.

The main objective of the present study is to evaluate the performance of different RANS turbulence models together with the VOF method in simulating breaking waves past a vertical cylinder. The paper is organized as follows: first, the governing equations for the numerical model are presented, followed by the grid and time-step refinement studies. Then, six simulations cases with different turbulence models are performed to predict the surface elevations and breaking wave forces on the vertical cylinder. The present numerical results are compared with the published experimental data from Irschik et al. (2005), which was presented by Choi et al. (2015). Subsequently, time-averaged velocity profiles and turbulent behavior are discussed in details. Finally, conclusions are drawn based on the present numerical results.

2. Numerical method

The numerical simulations are conducted using OpenFOAM together with a wave generation toolbox waves2Foam. The governing equations, turbulence models, free surface modelling method and numerical scheme are presented in this section.

2.1. Governing equations

The numerical model solves the motion of viscous fluid using the incompressible Reynolds-Averaged Navier-Stokes (RANS) equations:

$$\frac{\partial u_i}{\partial t}+u_j\frac{\partial u_i}{\partial x_j}=-\frac{1}{\rho}\frac{\partial p_{rgh}}{\partial x_i}+\nu\frac{\partial^2 u_i}{\partial x_j^2}-\frac{\partial \overline{u_i' u_j'}}{\partial x_j} \tag{1}$$

$$\frac{\partial u_i}{\partial x_i}=0 \tag{2}$$

where u_i are the Cartesian components of the fluid velocity, ρ is the fluid density, p_{rgh} is the pressure in excess of the hydrostatic pressure, and ν is the kinematic viscosity. $\overline{u_i' u_j'}$ is the Reynolds stress component, which is expressed using the Boussinesq approximation:

$$\overline{u_i' u_j'} = \nu_t \left(\frac{\partial u_i}{\partial x_j} + \frac{\partial u_j}{\partial x_i} \right) - \frac{2}{3} k \delta_{ij} \tag{3}$$

where ν_t is the turbulent kinematic viscosity, k is turbulent kinetic energy and δ_{ij} is the Kronecker delta.

2.2. Turbulence modelling

The additional transport equations should be used to yield a value for the turbulent kinematic viscosity ν_t to make the closure of RANS equations. In the present study, the $k-\omega$ *SST*, the buoyancy-modified $k-\omega SST$, the stabilized $k-\omega$ *SST* and the realizable $k-\varepsilon$ turbulence models are tested regarding their performance for predicting the interaction between the breaking wave and the vertical cylinder.

2.2.1. The $k-\omega$ SST model

The $k-\omega$ *SST* turbulence model was proposed by Menter et al. (2003) to effectively blend the $k-\varepsilon$ turbulence model in the far-field and $k-\omega$ turbulence model in the near-wall region. It avoids the problem that the $k-\omega$ turbulence model is very sensitive to the inlet free-stream turbulence properties. Besides, the $k-\omega$ *SST* turbulence model shows good behavior in predicting adverse pressure gradient and separation flow. Two advection-diffusion equations for turbulent kinetic energy k and specific rate of dissipation ω are expressed as:

$$\frac{\partial(\rho k)}{\partial t} + \frac{\partial(\rho u_i k)}{\partial x_i} = \frac{\partial}{\partial x_i}\left[(\mu + \sigma_k \mu_t) \frac{\partial k}{\partial x_i} \right] + P_k - \beta^* \rho \omega k \tag{4}$$

$$\frac{\partial(\rho \omega)}{\partial t} + \frac{\partial(\rho u_i \omega)}{\partial x_i} = \frac{\partial}{\partial x_i}\left[(\mu + \sigma_\omega \mu_t) \frac{\partial \omega}{\partial x_i} \right] + \alpha \rho S^2 - \beta \rho \omega^2 + 2(1-F_1) \frac{\rho \sigma_{\omega 2}}{\omega} \frac{\partial k}{\partial x_i} \frac{\partial \omega}{\partial x_i} \tag{5}$$

where the blending function F_1 is defined by

$$F_1 = \tanh\left\{ \left\{ \min\left[\max\left(\frac{\sqrt{k}}{\beta^* \omega y}, \frac{500\nu}{y^2 \omega} \right), \frac{4\rho\sigma_{\omega 2} k}{CD_{k\omega} y^2} \right] \right\}^4 \right\} \tag{6}$$

$$CD_{k\omega} = \max\left(2\frac{\rho\sigma_{\omega 2}}{\omega} \frac{\partial k}{\partial x_i} \frac{\partial \omega}{\partial x_i}, 10^{-10} \right) \tag{7}$$

where y is the distance to the nearest wall. The dynamic turbulent viscosity μ_t is defined as follows:

$$\mu_t = \frac{\rho a_1 k}{\max(a_1 \omega, S F_2)} \tag{8}$$

where $S = \sqrt{2 S_{ij} S_{ij}}$ is the invariant measure of the strain rate and F_2 is a second blending function defined by

$$F_2 = \tanh\left[\left[\max\left(\frac{2\sqrt{k}}{\beta^* \omega y}, \frac{500\nu}{y^2 \omega} \right) \right]^2 \right] \tag{9}$$

The production term $P_k = \min(G, 10\beta^* \rho k \omega)$, where G is given by

$$G = \mu_t \frac{\partial u_i}{\partial x_j} \left(\frac{\partial u_i}{\partial x_j} + \frac{\partial u_j}{\partial x_i} \right) \tag{10}$$

The constants of α_k, α_ω, α and β are blended using the equation:

$$\phi = F_1 \phi_1 + (1 - F_1) \phi_2 \tag{11}$$

The constants for this model are: $\beta^* = 0.09$, $\alpha_1 = 5/9$, $\beta_1 = 0.075$, $\sigma_{k1} = 0.85$, $\sigma_{\omega 1} = 0.5$, $\alpha_2 = 0.44$, $\beta_2 = 0.0828$, $\sigma_{k2} = 1$, $\sigma_{\omega 2} = 0.856$.

2.2.2. The buoyancy-modified $k-\omega$ SST model

Devolder et al. (2018) proposed a buoyancy-modified $k-\omega SST$ turbulence model. The buoyancy term G_b is added to the TKE equation to avoid the large production of turbulent kinetic energy due to the unbalanced pressure gradient and density gradient between water and air at the free surface. The two equations for k and ω are expressed as:

$$\frac{\partial(\rho k)}{\partial t} + \frac{\partial(\rho u_i k)}{\partial x_i} = \frac{\partial}{\partial x_i}\left[(\mu + \sigma_k \mu_t) \frac{\partial k}{\partial x_i} \right] + P_k + G_b - \beta^* \rho \omega k \tag{12}$$

$$\frac{\partial(\rho \omega)}{\partial t} + \frac{\partial(\rho u_i \omega)}{\partial x_i} = \frac{\partial}{\partial x_i}\left[(\mu + \sigma_\omega \mu_t) \frac{\partial \omega}{\partial x_i} \right] + \frac{\alpha}{\nu_t} G - \beta \rho \omega^2 + 2(1-F_1) \frac{\rho \sigma_{\omega 2}}{\omega} \frac{\partial k}{\partial x_i} \frac{\partial \omega}{\partial x_i} \tag{13}$$

The buoyancy term G_b is defined as:

$$G_b = -\nu_t \alpha_{\beta s} \frac{\partial \rho}{\partial x_i} g_i \tag{14}$$

where $\alpha_{\beta s}$ is the buoyancy modification coefficient and the default value is 1.176.

2.2.3. The stabilized $k-\omega$SST model

Larsen and Fuhrman (2018) proposed a stabilized $k-\omega SST$ closure model by adding buoyancy production term G_b and stress-limiting modifications to the $k-\omega SST$ (Menter et al., 2003) model. This turbulence model aims to avoid non-physical exponential growth of the turbulent kinetic energy and eddy viscosity in the nearly potential flow region. The turbulent kinetic energy equation and the specific rate of dissipation equation are the same with Equation (12) and Equation (5), respectively; however, the buoyancy modification coefficient $\alpha_{\beta s}$ is 1.36. The eddy viscosity is redefined according to

$$\nu_t = \frac{a_1 k}{\max\left(a_1 \omega, F_2 \sqrt{P_0}, a_1 \lambda_2 \frac{\beta}{\beta^* \alpha} \frac{P_0}{P_\Omega} \omega \right)} \tag{15}$$

where a third argument has been added within the max function. λ_2 is an additional stress limiter coefficient, and the default value is 0.05. $P_0 = 2 S_{ij} S_{ij}$, and $P_\Omega = 2\Omega_{ij}\Omega_{ij}$. The mean strain rate tensor is $S_{ij} = \frac{1}{2}\left(\frac{\partial u_i}{\partial x_j} + \frac{\partial u_j}{\partial x_i} \right)$ and the mean rotation rate tensor is $\Omega_{ij} = \frac{1}{2}\left(\frac{\partial u_i}{\partial x_j} - \frac{\partial u_j}{\partial x_i} \right)$. Note that the new addition to the limiter in Equation (15) will become active only in a region of nearly potential flow where $P_0 \gg P_\Omega$. The other details of model parameters' definitions and coefficients are the same as the $k-\omega SST$ turbulence model (Menter et al., 2003).

2.2.4. The realizable $k-\varepsilon$model

The realizable $k-\varepsilon$ model developed by Shih et al. (1995) differs from the standard $k-\varepsilon$ model in two ways. First, the realizable $k-\varepsilon$ model contains a new formulation for the turbulent viscosity: C_μ is a variable instead of constant. The second difference is that a new transport equation for the dissipation rate ε is applied, which is derived from an exact equation for the transport of the mean-square vorticity fluctuation. The realizable $k-\varepsilon$ model exhibits superior performance for spreading rate of jets, boundary layers under strong adverse pressure gradients and involving rotation. Two equations of k and ε in the realizable $k-\varepsilon$ model are defined as

$$\frac{\partial(\rho k)}{\partial t} + \frac{\partial(\rho k u_j)}{\partial x_j} = \frac{\partial}{\partial x_j}\left[\left(\mu + \frac{\mu_t}{\sigma_k} \right) \frac{\partial k}{\partial x_j} \right] + P_k + P_b - \rho\varepsilon - Y_M + S_k \tag{16}$$

$$\frac{\partial(\rho \varepsilon)}{\partial t} + \frac{\partial(\rho \varepsilon u_j)}{\partial x_j} = \frac{\partial}{\partial x_j}\left[\left(\mu + \frac{\mu_t}{\sigma_\varepsilon} \right) \frac{\partial \varepsilon}{\partial x_j} \right] + \rho C_1 S \varepsilon - \rho C_2 \frac{\varepsilon^2}{k + \sqrt{\nu\varepsilon}} + C_{1\varepsilon} \frac{\varepsilon}{k} C_{3\varepsilon} P_b + S_\varepsilon \tag{17}$$

where $C_1 = \max\left[0.43, \frac{\eta}{5+\eta} \right]$, $\eta = \frac{Sk}{\varepsilon}$. P_k and P_b represents the generation of turbulence kinetic energy due to the mean velocity gradients and the buoyancy respectively. The turbulent viscosity is computed using

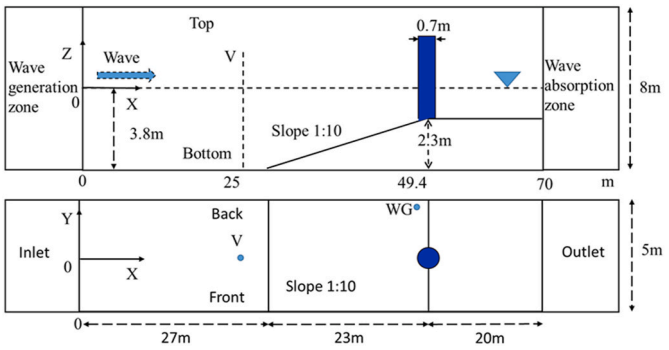

Fig. 1. Sketch of the numerical wave tank: side view (top); plan view (bottom).

$$\mu_t = \rho C_\mu \frac{k^2}{\varepsilon} \tag{18}$$

and C_μ is given by

$$C_\mu = \frac{1}{A_0 + A_s U^* \frac{k}{\varepsilon}} \tag{19}$$

The constants of this model are $C_{1\varepsilon} = 1.44$, $C_2 = 1.9$, $\sigma_k = 1.0$, $\sigma_\varepsilon = 1.2$, $A_0 = 4.0$.

2.3. Free surface capture

The VOF method (Hirt and Nichols, 1981) is used to capture the interface between the air and the water. The method is based on a volume fraction coefficient α, which is 0 for air and 1 for water. The volume fraction is solved by following the advection equation:

$$\frac{\partial \alpha}{\partial t} + \frac{\partial (\alpha u_i)}{\partial x_i} + \frac{\partial [\alpha(1-\alpha) u_{ir}]}{\partial x_i} = 0 \tag{20}$$

where u_{ir} is the relative velocity between the water phase and the air phase. The density and kinematic viscosity at the interface are obtained by a weighted value based on the volume fraction coefficient α.

$$\begin{cases} \rho = \alpha \rho_w + (1-\alpha)\rho_a \\ \nu = \alpha \nu_w + (1-\alpha)\nu_a \end{cases} \tag{21}$$

where ρ_w and ρ_a denote the densities of water and air; ν_w and ν_a are the kinematic viscosity coefficients of water and air.

2.4. Relaxation method

The wave relaxation algorithm presented by Jacobsen et al. (2012) is applied to generate and absorb waves in the numerical wave tank (NWT). The velocity and the wave surface elevation ramp up to the target values according to the wave theory. The relaxation function is expressed by

$$\varphi = \gamma_R \varphi_{\text{computed}} + (1-\gamma_R)\varphi_{\text{target}} \tag{22}$$

where φ is either velocity u_i or volume fraction α, and the weighting factor γ_R is defined as:

$$\gamma_R = 1 - \frac{\exp(\chi_R^{3.5}) - 1}{\exp(1) - 1}, \chi_R \in [0, 1] \tag{23}$$

2.5. Numerical scheme

The finite volume method (FVM) is used to solve the Navier–Stokes equations. The PISO-SIMPLE (PIMPLE) algorithm is used to deal with the pressure and velocity coupling. The second-order implicit Crank-Nicolson scheme is applied for the discretization of the time domain. The second-order Gauss integration with linear interpolation combining

Table 1
Resolutions of three different meshes.

Mesh	Coarse mesh	Medium mesh	Fine mesh
The elements number	5791152	7787600	8564864
Minimum gird size along cylinder circle (m)	0.0137	0.0122	0.0110
Minimum gird size normal to the cylinder (m)	0.003	0.003	0.003
At wave generator (m) Max (Δx Δy,Δz)	(0.15, 0.1, 0.08)	(0.12, 0.08, 0.05)	(0.1, 0.01, 0.045)
Maximum Courant number	0.5	0.5 0.3	0.5
The Maximum forces (kN)	11.71	11.95 11.73	12.21

'limitedLinear 1' limiter function is used for the convective terms. The second-order Gauss integration with linear interpolation is employed for the diffusive terms. The pressure is solved by the generalised geometric-algebraic multi-grid (GAMG) numerical method with Diagonal-based Incomplete Cholesky (DIC) preconditioner.

3. Numerical implementation

3.1. Computational domain

The setup of the computational domain is done according to the experimental tests conducted by Irschik et al. (2005). The dimensions of the numerical wave tank (NWT) are 120.0 m long, 5 m wide and 8 m height, as shown in Fig. 1. A cylinder with the diameter of $D = 0.7$ m is installed with its central axis at the edge of the slope (1:10). The water depth of NWT is 3.8 m. A wave gauge (WG) is used to measure the free surface elevation near the sidewall along the frontline of the cylinder. Both the wave generation zone and the absorption zone are one wavelength long. The wave height of $H = 1.3$m and the wave period of $T = 4.0$s is generated in the NWT for all the simulation cases.

3.2. Boundary conditions

The no-slip condition for velocity and zero gradient condition for pressure are employed in the front, back, bottom and cylinder's surface boundaries. The wall functions are employed to simulate characteristics of the boundary layer. The dimensionless wall distance y^+ ($y^+ = \frac{d_n u_t}{\nu}$, where d_n is the normal distance to the wall, u_t is the friction velocity and ν is the kinematic viscosity) is in the range of 40–200 for the present simulation. The water velocity is obtained from the wave theory and the air velocity is zero at the inlet boundary. At the outlet boundary, both the water and air velocities are set to zero. The pressures are specified as zero gradient condition at the inlet and outlet boundaries. On the top domain, the *pressureInletOutletVelocity* is applied to the velocity, which means that the velocity for the inflow is calculated from the flux in the patch-normal direction and the velocity for the outflow is set as the zero normal gradient boundary condition. The *totalPressure* is used to calculated pressure on the top boundary, which is obtained by subtracting the dynamic pressure from the total pressure, expressed as follows:

$$p_p = p_0 - 0.5|\mathbf{u}|^2 \tag{24}$$

where p_0 is total pressure and $\mathbf{u}$ is the mean velocity vector.

3.3. Convergence studies

The grid and time-step refinement studies are carried out in terms of the horizontal breaking wave forces on the cylinder and the free surface elevations at WG location with the $k-\omega$ *SST* turbulence model. Two strategies are employed to optimize the computational cost. Firstly, the non-uniform grid which is refined in the vicinity of the cylinder and the free surface is used. Secondly, the adaptive time-step approach based on

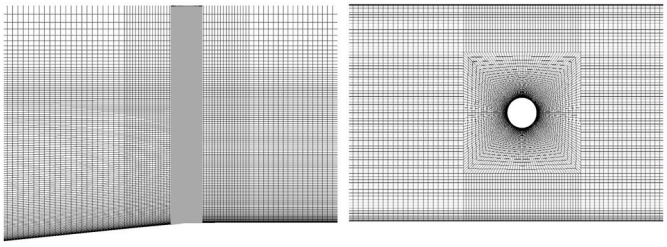

Fig. 2. The view of medium mesh around the cylinder: side view (left); top view (right).

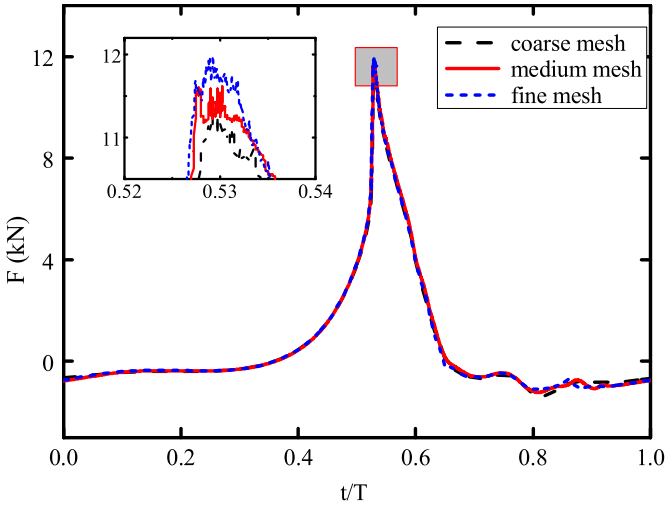

Fig. 3. Horizontal breaking wave forces on the cylinder with different grid resolutions.

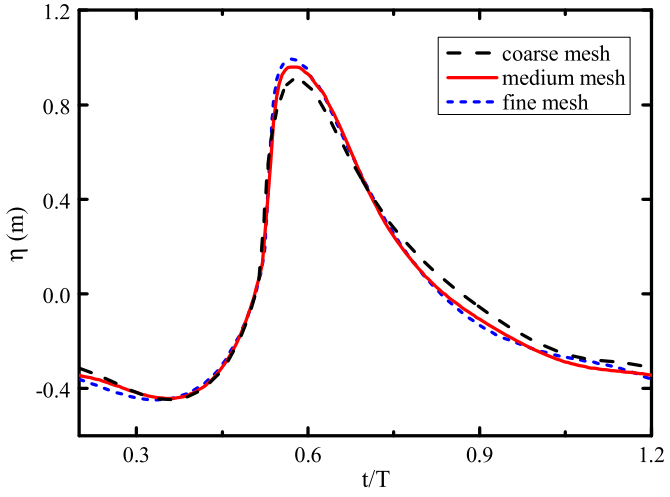

Fig. 4. Free surface elevations at WG location with different grid resolutions.

maximum Courant number (Comax) is employed. Different meshes and Courant number are shown in Table 1. Moreover, the side view and top view of the medium mesh around the vertical cylinder are also shown in Fig. 2.

Figs. 3 and 4 show the total horizontal breaking wave forces F on the vertical cylinder and the free surface elevations η at WG location with three sets of meshes over one wave period, respectively. The relative variation in peak values of F between the fine mesh and the medium mesh is 2.2%. The difference in the free surface elevation between the fine mesh and the medium mesh is 3.0%. The grid resolution of the medium mesh is considered sufficiently accurate for the present simulations. Moreover, the refinement study on time-step is also carried out by changing Comax. It can be seen from Figs. 5 and 6 that there is no significant change for the peaks of F and η when Comax decreases from 0.5 to 0.3. Therefore, the medium mesh with Comax = 0.5 is considered to give satisfactory numerical accuracy and will be used in subsequent

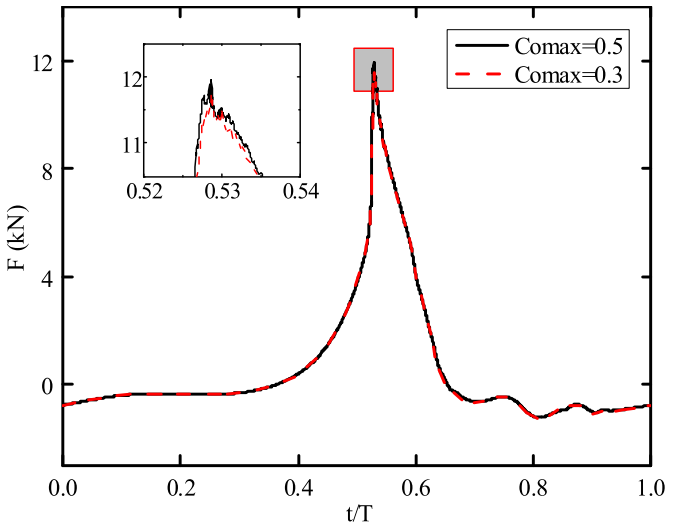

Fig. 5. Horizontal breaking wave forces on the cylinder with different Courant number.

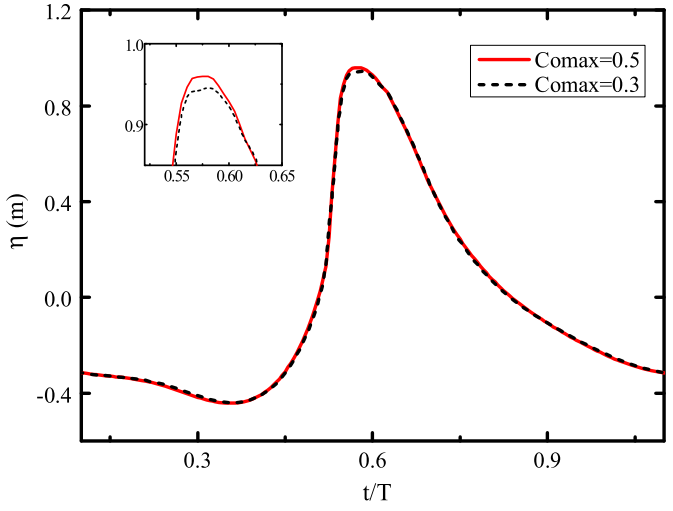

Fig. 6. Surface elevations at WG location with different Courant number.

Table 2
Details of the setups in different simulation cases. The incident wave parameters are $H = 1.3m$, $T = 4.0s$.

Cases	Turbulent models	Breaker pointsx_b(m)	Max force (kN)
1	No turbulence model	46.39	8.33
2	Stabilized $k-\omega$ $SST(\lambda_2 = 0.05, \alpha_{\beta s} = 1.36)$	46.40	8.13
3	Buoyancy-modified$k-\omega$ $SST(\alpha_{\beta s} = 1.176)$	46.50	8.52
4	Modified stabilized $k-\omega$ $SST(\lambda_2 = 0.05, \alpha_{\beta s} = 0)$	48.40	11.95
5	$k-\omega$ SST	49.43	11.95
6	Realizable $k-\varepsilon$	Behind cylinder	9.10

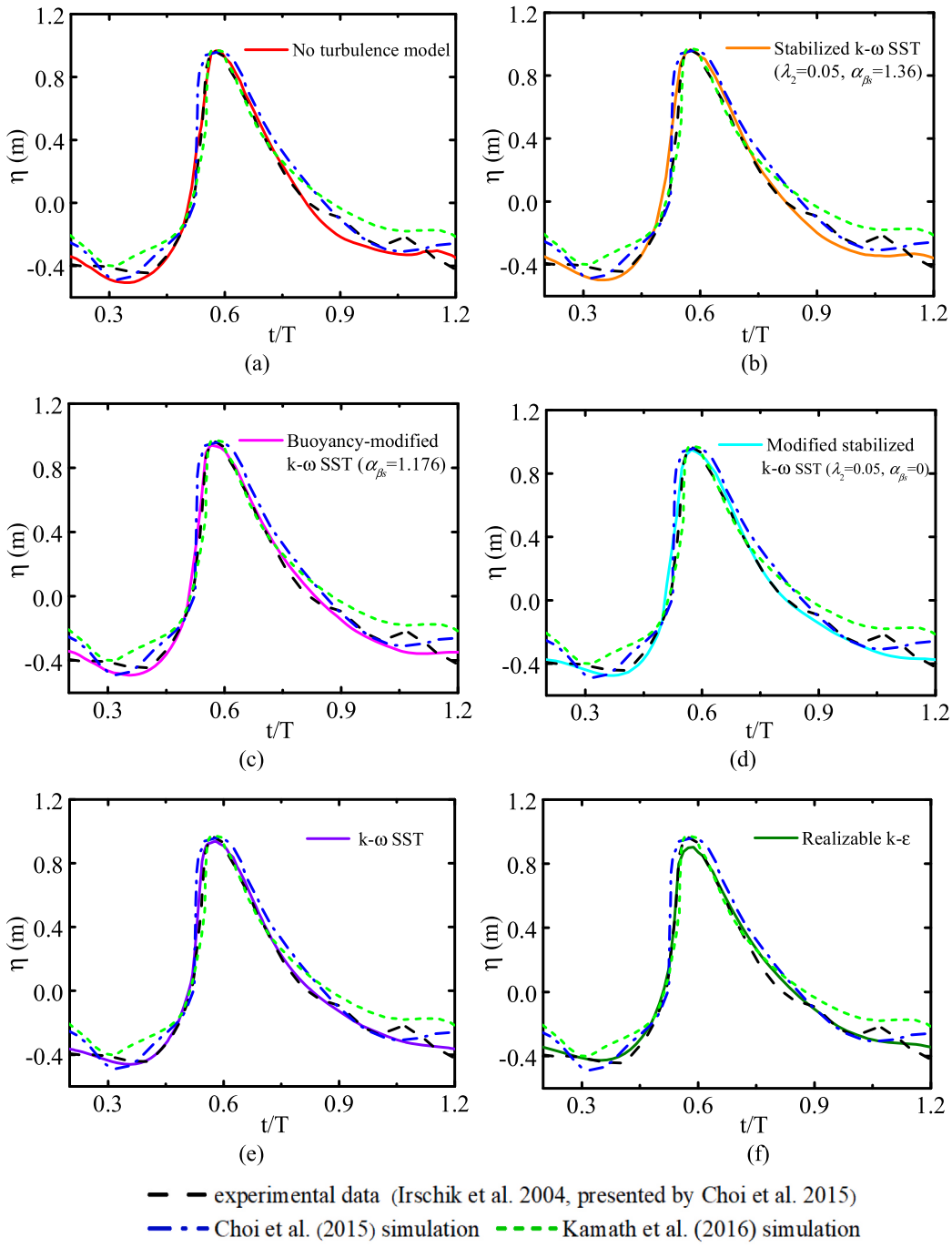

Fig. 7. Numerically obtained surface elevations averaged over 10 wave periods at WG location with different turbulence models, including (a) no turbulence model (b) stabilized $k-\omega$ *SST* ($\lambda_2 = 0.05$, $\alpha_{\beta s} = 1.36$) (c) buoyancy-modified $k-\omega$ *SST* ($\alpha_{\beta s} = 1.176$) (d) modified stabilized $k-\omega$ *SST* ($\lambda_2 = 0.05$, $\alpha_{\beta s} = 0$) (e) $k-\omega$ *SST* (f) realizable $k-\varepsilon$ turbulence models.

simulations.

4. Results and discussion

In this study, six simulation cases are conducted, as listed in Table 2. For Case 4, the modified stabilized $k-\omega$ *SST* turbulence model ($\lambda_2 = 0.05$, $\alpha_{\beta s} = 0$) is employed to investigate the effects of buoyancy modification coefficient and the stress limiter coefficient on the numerical results by comparing with Case 2 and Case 5. The numerical results of free surface elevations and horizontal wave forces on the cylinder are compared with experimental data from Irschik et al. (2005) (presented by Choi et al. (2015)) to evaluate the performance of different turbulence models. Moreover, the time-averaged velocity, breaker locations and the turbulent behavior are discussed. All the present simulations are performed for a minimum duration of 40 wave periods, and the last ten wave periods are averaged and used as the present results.

4.1. Free surface elevations and breaking wave forces

Fig. 7 shows the comparison of surface elevations η at Location WG (see Fig. 1) between the numerical results predicted by different numerical models and the experimental data over one wave period. All the models generally show a good agreement in the surface elevations with

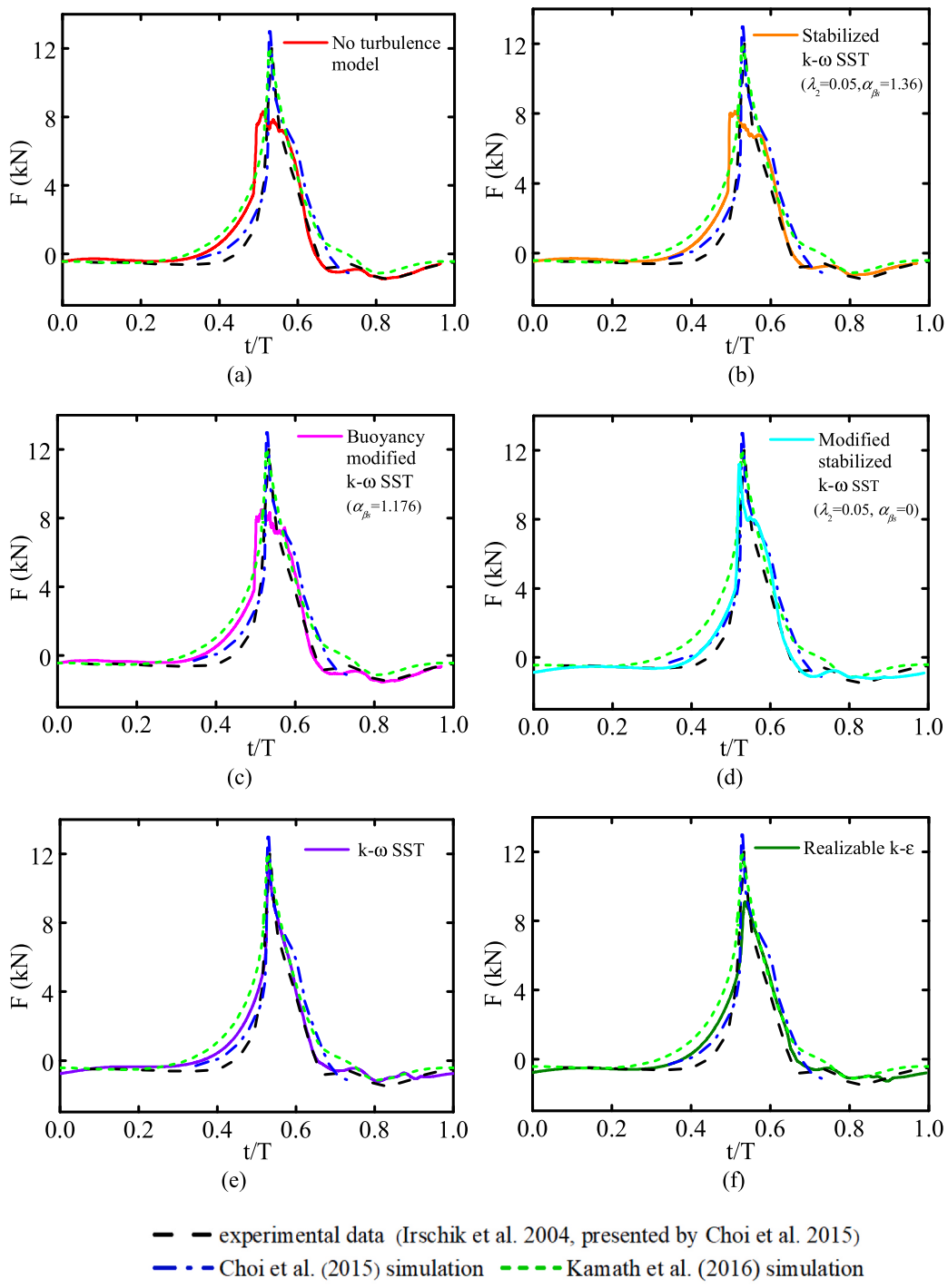

Fig. 8. Numerically obtained horizontal breaking wave forces averaged over 10 wave periods with different turbulence models, including (a) no turbulence model (b) stabilized $k-\omega$ *SST* ($\lambda_2 = 0.05$, $\alpha_{\beta s} = 1.36$) (c) buoyancy-modified $k-\omega$ *SST* ($\alpha_{\beta s} = 1.176$) (d) modified stabilized $k-\omega$ *SST* ($\lambda_2 = 0.05$, $\alpha_{\beta s} = 0$) (e) $k-\omega$ *SST* (f) realizable $k-\varepsilon$turbulence models.

the experimental data. The modified stabilized $k-\omega$ *SST* ($\lambda_2 = 0.05$, $\alpha_{\beta s} = 0$) and the $k-\omega$ *SST* turbulence models agree best with the experimental data except for the slight discrepancy at $t/T = 1.05$. In the experiment, the wave gauges were installed near the wave tank sidewall to avoid the influence of the measurement equipment on the waves. The interactions between the wave tank sidewall and the wave gauges, as well as the interactions between different wave gauges, can affect the nearby free surface. In Fig. 7(a) and (b), it can be observed that the stabilized $k-\omega$*SST* ($\lambda_2 = 0.05$, $\alpha_{\beta s} = 1.36$) turbulence model gives similar results to the no turbulence model, and the peak of surface elevations are predicted accurately. However, the corresponding numerical values are lower than the experimental data at $t/T = 0.3$ and $t/T = 0.9$. This is due to that the wave breaks prematurely before it arrives at the vertical cylinder. In addition, the predicted peaks of the surface elevations using turbulence models (the $k-\omega$ *SST* turbulence model, the buoyancy-modified $k-\omega$*SST* turbulence model, the stabilized $k-\omega$ *SST* turbulence model, the modified stabilized $k-\omega$ *SST*turbulence model and the realizable $k-\varepsilon$ turbulence model) are slightly lower than that without turbulence model. According to the law of conservation of energy, the kinetic energy and potential energy transform to each other

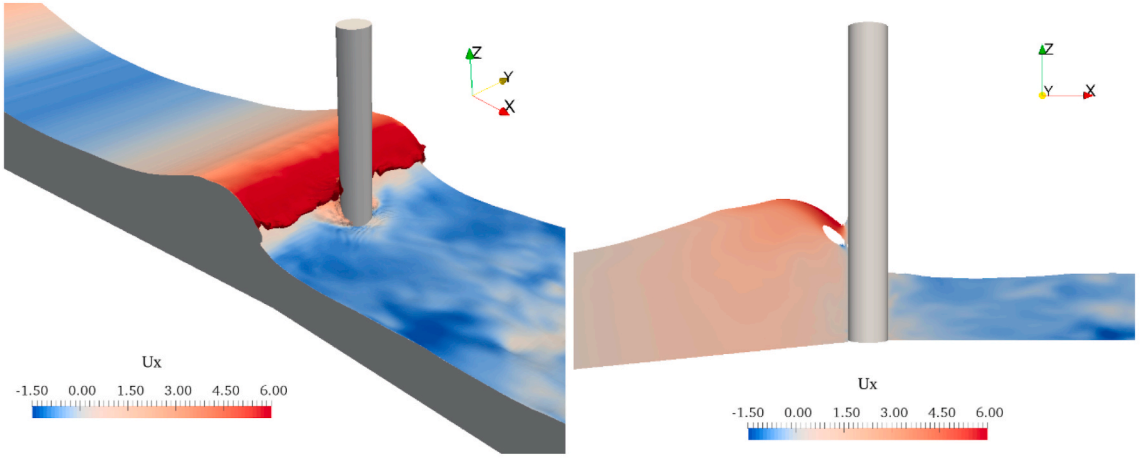

(a) No turbulence model

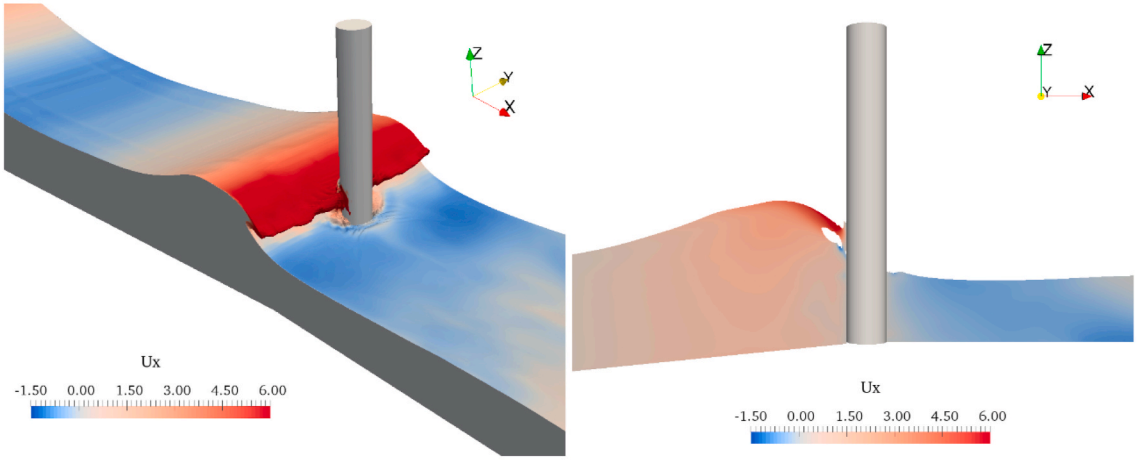

(b) Stabilized $k-\omega$ SST (λ_2=0.05 , $\alpha_{\beta s}$=1.36)

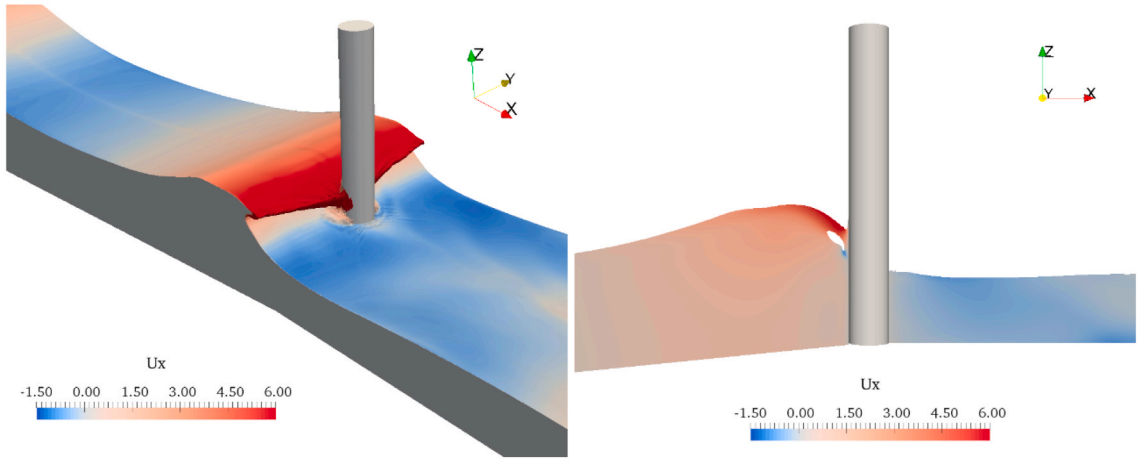

(c) Buoyancy-modified $k-\omega$ SST ($\alpha_{\beta s}$=1.176)

Fig. 9. Snapshots of the waves crest front touching the cylinder with the horizontal velocity contours using different turbulence models (a) no turbulence model (b) stabilized $k-\omega$ SST (λ_2 = 0.05, $\alpha_{\beta s}$ = 1.36) (c) buoyancy-modified $k-\omega$ SST ($\alpha_{\beta s}$ = 1.176) (d) modified stabilized $k-\omega$ SST (λ_2 = 0.05, $\alpha_{\beta s}$ = 0) (e) $k-\omega$ SST (f) realizable $k-\varepsilon$.

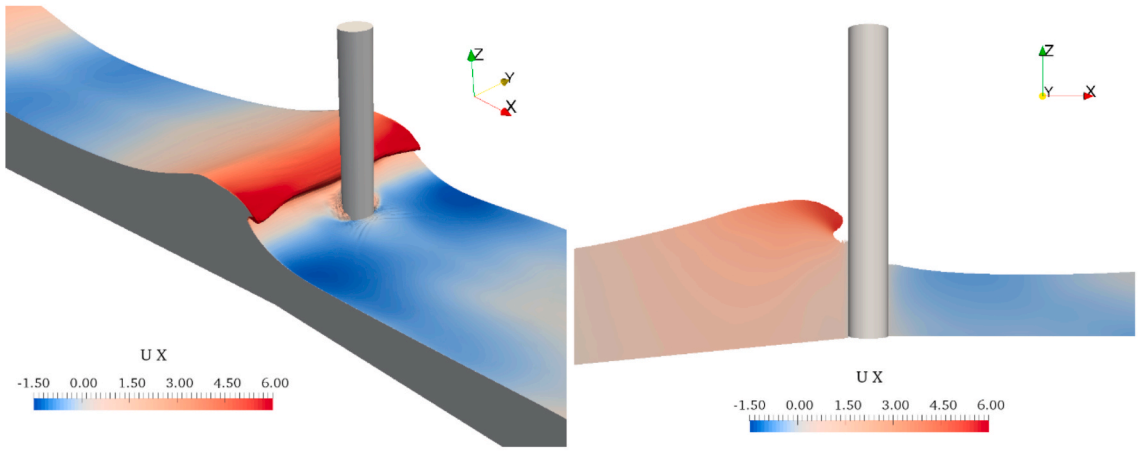

(d) Modified stabilized $k-\omega$ *SST* (λ_2=0.05 , $\alpha_{\beta s}$=0)

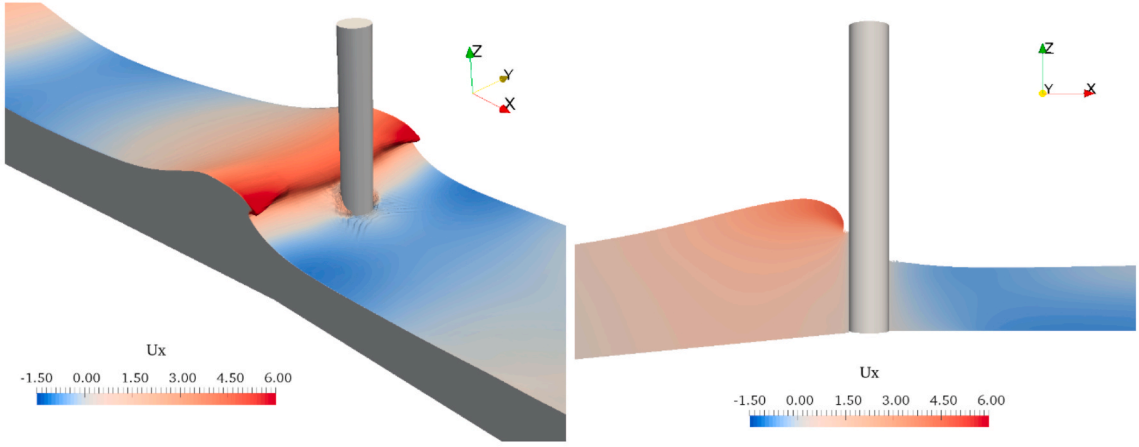

(e) $k-\omega$ *SST*

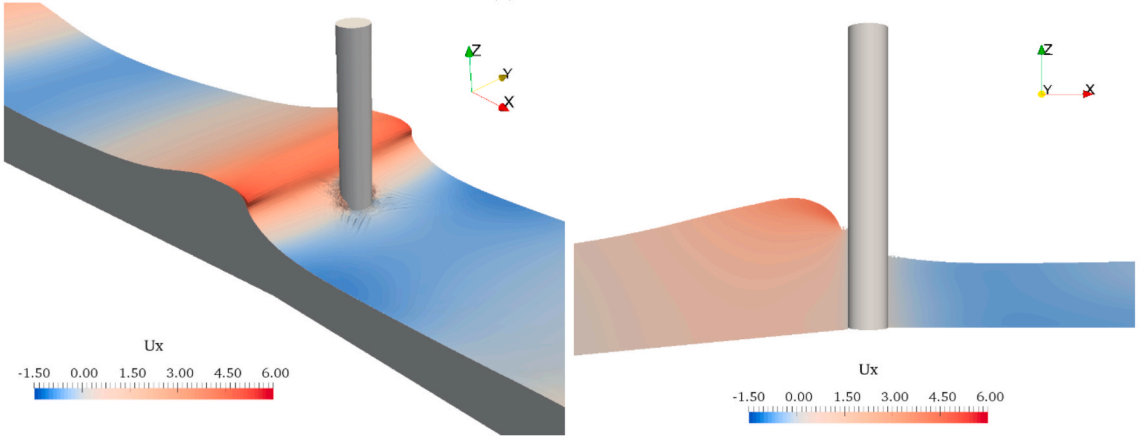

(f) Realizable $k-\varepsilon$

Fig. 9. (*continued*).

during the wave propagation process. When the turbulence model is applied, the turbulent kinetic energy is generated by extracting energy from the total kinetic energy, and will dissipate due to the viscous force and disappear eventually. Therefore, the application of turbulence models reduces the total kinetic energy. As a result, the slightly smaller peaks of surface elevations are observed in the numerical results with the turbulence models.

Fig. 8 presents the comparison of the numerical horizontal breaking wave forces F_T on the cylinder and the corresponding experimental data over one wave period. Fig. 9 shows the snapshots of the waves crest front touching the cylinder with the horizontal velocity contours using different turbulence models. The stabilized $k-\omega$ *SST* ($\lambda_2 = 0.05$, $\alpha_{\beta s} = 1.36$) turbulence model, the modified stabilized $k-\omega$ *SST* ($\lambda_2 = 0.05$,$\alpha_{\beta s} = 0$) turbulence model, the buoyancy-modified $k-\omega$ *SST* turbulence model ($\alpha_{\beta s} = 1.176$) and the no turbulence model give a similar prediction for the breaking wave forces. The peaks of wave forces are lower and appear earlier than the experimental measurement. The reason is that the stabilized $k-\omega$ *SST* ($\lambda_2 = 0.05$, $\alpha_{\beta s} = 1.36$)

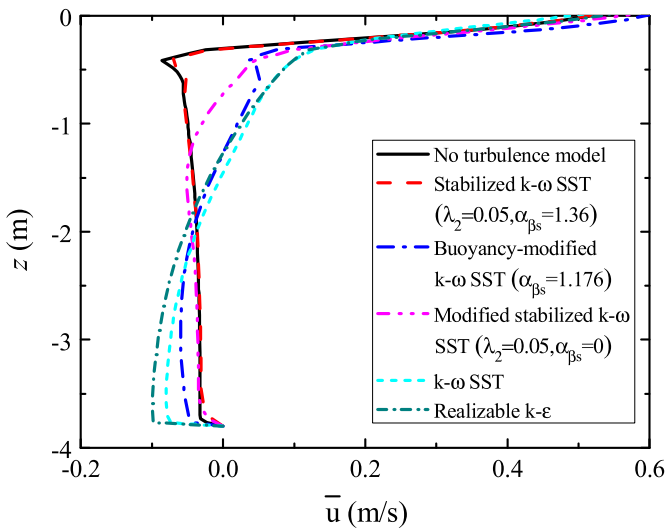

Fig. 10. Comparison of time averaged horizontal velocity profiles with different turbulence models at x = 25m (Location V).

turbulence model and the buoyancy-modified $k-\omega$ *SST* turbulence model ($\alpha_{\beta s}$ = 1.176) produce a very low value of TKE (see Fig. 11). Therefore, the turbulence effect is very limited, showing similar behavior with the no turbulence model. The waves breaking prematurely cause an overturn wave tongue hitting the cylinder, as shown in Fig. 9(a) and (b). In Fig. 8(e), the$k-\omega$ *SST* turbulence model predicts the breaking wave force reasonably well as compared with the experimental data. Both the first peak and the second peak of the breaking wave force are predicted accurately. The wave front is almost vertical when it impacts on the cylinder as shown in Fig. 9(e). Additionally, the wave force computed by the realizable $k-\varepsilon$ turbulence model is underestimated as compared with the experimental data. This could imply that the wave does not break before hitting the cylinder. The wave front is inclined when it reaches the cylinder (see Fig. 9(f)), which cause the small wave force.

Fig. 8 shows that the computed rise-time of the wave force is ahead of the experimental rise-time around t/T = 0.4. This can be explained as the assumptions of incompressible flow and rigidly fixed cylinders applied in the present numerical simulations. However, in the experiment, cylinder vibration, the compressibility of the flow and water droplets on the surface of the cylinder can influence the rise-time. Similar phenomena can also be found in the validation studies done by Liu et al. (2019), Kamath et al. (2016) and Bihs et al. (2016).

Overall, the breaking wave force on the cylinder depends not only on the wave elevation but also on the wave front shape when it hits the cylinder. A slight change in the predicted wave breaking point, may have a significant effect on the value of the wave force. The $k-\omega$ *SST* turbulence model with the VOF method shows reasonably good performance in predicting both surface elevations and wave forces on the vertical cylinder.

4.2. Averaged velocity profiles

Fig. 10 shows the comparison of time-averaged horizontal velocities with different turbulence models at Location V (see Fig. 1). The position of V is located in the flat bottom section of the NWT at x = 25m. The vertical axis denotes the vertical coordinates in the NWT. The horizontal axis represents the values of averaged horizontal velocities. At Location V, all the numerical models can capture the basic variation of the averaged horizontal velocity. It is negative throughout the majority of the water column and becomes positive near the free water surface. The mean velocities are small near the bottom of the water column and increase gradually when the position approaches the free surface. Meanwhile, negative velocity gradients are observed as the water depth increases when using the no turbulence model, stabilized $k-\omega$ *SST* (λ_2 = 0.05, $\alpha_{\beta s}$ = 1.36) turbulence model and modified stabilized $k-\omega$ *SST* (λ_2 = 0.05,$\alpha_{\beta s}$ = 0) turbulence model. While velocity gradients are positive for the $k-\omega$ *SST* turbulence model and the realizable $k-\varepsilon$ turbulence model at the same location. As aforementioned, the function of the buoyancy term is to avoid the large production of turbulent kinetic energy due to the unbalanced pressure gradient and density gradient between the water and air phases at the free surface. It means that the buoyancy term mainly affects the flow characteristics near the free surface. Therefore, the time-averaged horizontal velocity profiles calculated by turbulence models with buoyancy term (stabilized $k-\omega SST$ (λ_2 = 0.05, $\alpha_{\beta s}$ = 1.36) and the buoyancy-modified $k-\omega$ *SST* ($\alpha_{\beta s}$ = 1.176)) show similar trend near the free surface (see the free surface region in Fig. 10). While the stress limiter coefficient can affect the entire flow field. This can be verified by comparing the stabilized $k-\omega$ *SST* (λ_2 = 0.05, $\alpha_{\beta s}$ = 1.36) and the modified stabilized $k-\omega$ *SST* (λ_2 = 0.05, $\alpha_{\beta s}$ = 0), which shows the similar time-averaged horizontal velocity profiles under the free surface (see the region of $z < -1.5$ m in Fig. 10). Eventually, when the buoyancy modification coefficient and the stress limiter coefficient are employed simultaneously in the stabilized $k-\omega$ *SST* (λ_2 = 0.05, $\alpha_{\beta s}$ = 1.36), the time-averaged horizontal velocity profile is almost same with that in the case of no turbulence model in the vicinity and underneath the free surface.

4.3. Turbulent behavior

In order to identify the turbulent behaviour of the different turbulence models, contours of the turbulent kinetic energy k around the breaking point are depicted in Fig. 11. The stabilized $k-\omega$ *SST* (λ_2 = 0.05,$\alpha_{\beta s}$ = 1.36) turbulence model and the buoyancy-modified $k-\omega$ *SST* ($\alpha_{\beta s}$ = 1.176) turbulence model show very small values of TKE in the entire fluid domain before the wave breaking, see Fig. 11(a) and (b). This is attributed to the function of the limiter inside the buoyancy term of TKE equation. The positions of wave breaking points predicted by the stabilized $k-\omega$ *SST* (λ_2 = 0.05, $\alpha_{\beta s}$ = 1.36) turbulence model and the buoyancy-modified $k-\omega$ *SST* ($\alpha_{\beta s}$ = 1.176) turbulence model are ahead of the other turbulence models. The TKE predicted by the modified stabilized $k-\omega$ *SST* (λ_2 = 0.05, $\alpha_{\beta s}$ = 0) turbulence model presents a high value on the wave crest of the breaking point (Fig. 11(c)). However, the largest TKE is obtained from the $k-\omega$ *SST* turbulence model near the free surface, which can be seen in Fig. 11(d). It causes that the total kinetic energy is diffused and dissipated during the wave propagation. Finally, the breaking point predicted by the $k-\omega$ *SST* turbulence model is beyond the breaking points predicted by the stabilized $k-\omega$ *SST* (λ_2 = 0.05, $\alpha_{\beta s}$ = 1.36) turbulence model, the buoyancy-modified $k-\omega SST$ ($\alpha_{\beta s}$ = 1.176) turbulence model and the modified stabilized $k-\omega SST$ (λ_2 = 0.05, $\alpha_{\beta s}$ = 0) turbulence model. Fig. 11(d) shows that the position of wave breaking point predicted by the $k-\omega$ *SST* model is at the front surface of the vertical cylinder, which is consistent with the predictions by Bihs et al. (2016), Kamath et al. (2016) and Choi et al. (2015), as well as the experimental data by Irschik et al. (2005). In the realizable $k-\varepsilon$ turbulence model, the more kinetic energy is converted into TKE in the entire fluid domain (see Fig. 11(e)). The total kinetic energy loss makes the wave to reach the cylinder without breaking. This is consistent with the aforementioned discussion that the surface elevation and the breaking wave force predicted by the realizable $k-\varepsilon$ turbulence model are underestimated as compared to the experimental data.

Furthermore, contours of the turbulent kinematic viscosity ν_t using different turbulence models are depicted in Fig. 12. In the cases of the turbulence models with buoyancy modified term (see Fig. 12(a) and (b)), ν_t around the free surface goes to zero. When the stress limiter coefficient λ_2 is also employed (see Fig. 12(a)), ν_t is zero not only on the free surface but also inside the fluid before the breaking point. This

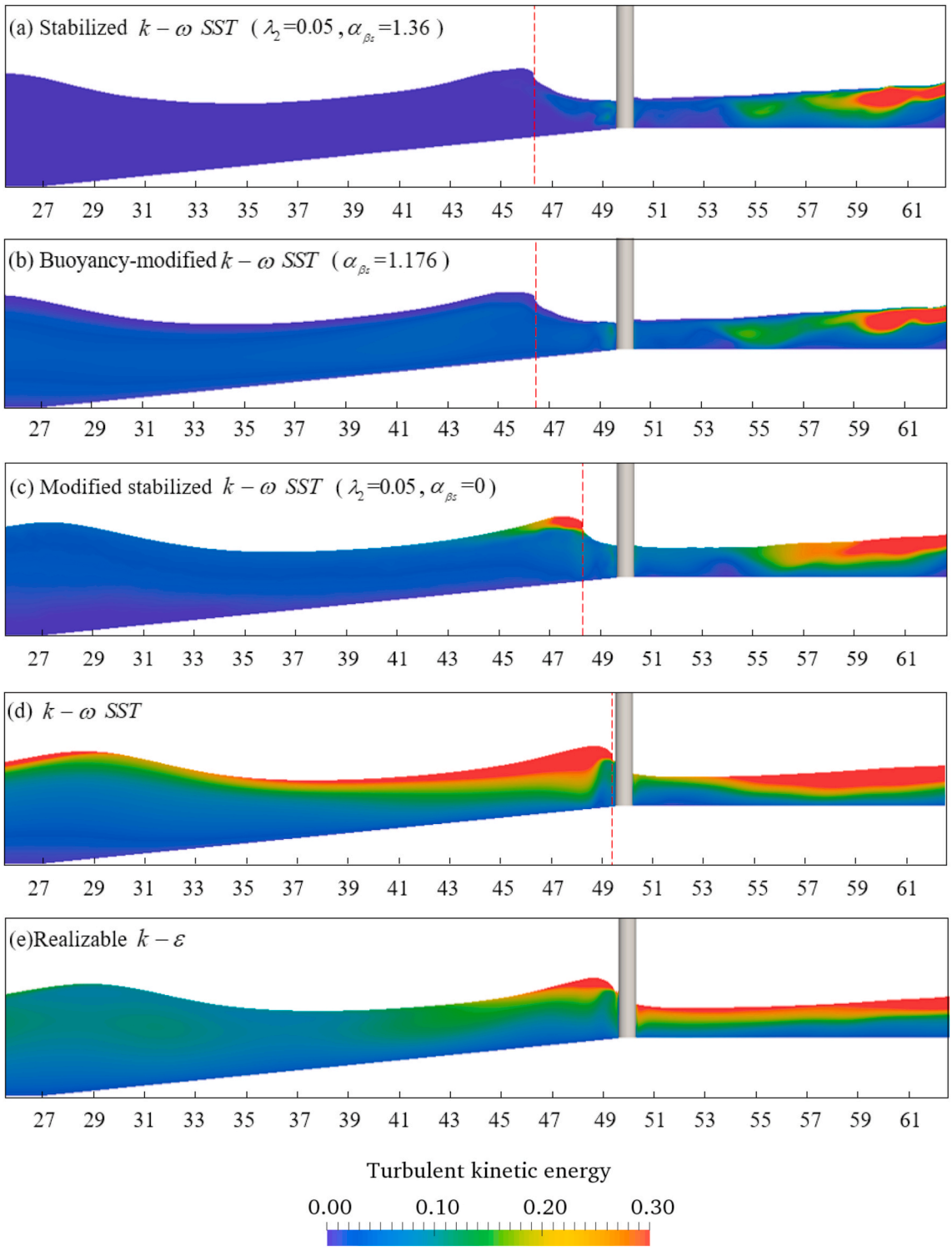

Fig. 11. Snapshots of the turbulent kinetic energy k (m^2/s^2) at the breaking point with the (a) stabilized $k-\omega$ *SST* ($\lambda_2 = 0.05, \alpha_{\beta s} = 1.36$) (b) buoyancy-modified $k-\omega$ *SST* ($\alpha_{\beta s} = 1.176$) (c) modified stabilized $k-\omega$ *SST* ($\lambda_2 = 0.05, \alpha_{\beta s} = 0$) (d) $k-\omega$ *SST* (e) realizable $k-\varepsilon$. The red dash lines present the position of breaking point. (For interpretation of the references to colour in this figure legend, the reader is referred to the Web version of this article.)

means that there is no obvious turbulent effect in the flow field before the breaking point. The performance of the stabilized $k-\omega$ *SST* ($\lambda_2 = 0.05$, $\alpha_{\beta s} = 1.36$) and the no turbulence model are almost identical in terms of the surface elevations at Location WG, the wave forces on the cylinder and the locations of breaking points. The comparison between Fig. 12(c) and (d) shows that the stress limiter coefficient λ_2 significantly reduces ν_t in the entire flow field. The buoyancy modification coefficient $\alpha_{\beta s}$ mainly affects the ν_t on the free surface based on the comparison of Fig. 12(b) and (d). The realizable $k-\varepsilon$ turbulence model predicts relatively large ν_t in the active flow field, leading to the non-breaking wave before reaching the cylinder.

In summary, both the stress limiter coefficient λ_2 and the buoyancy modification coefficient $\alpha_{\beta s}$ have an important influence on predictions of free surface elevation, breaking wave force, TKE and ν_t. The turbu-

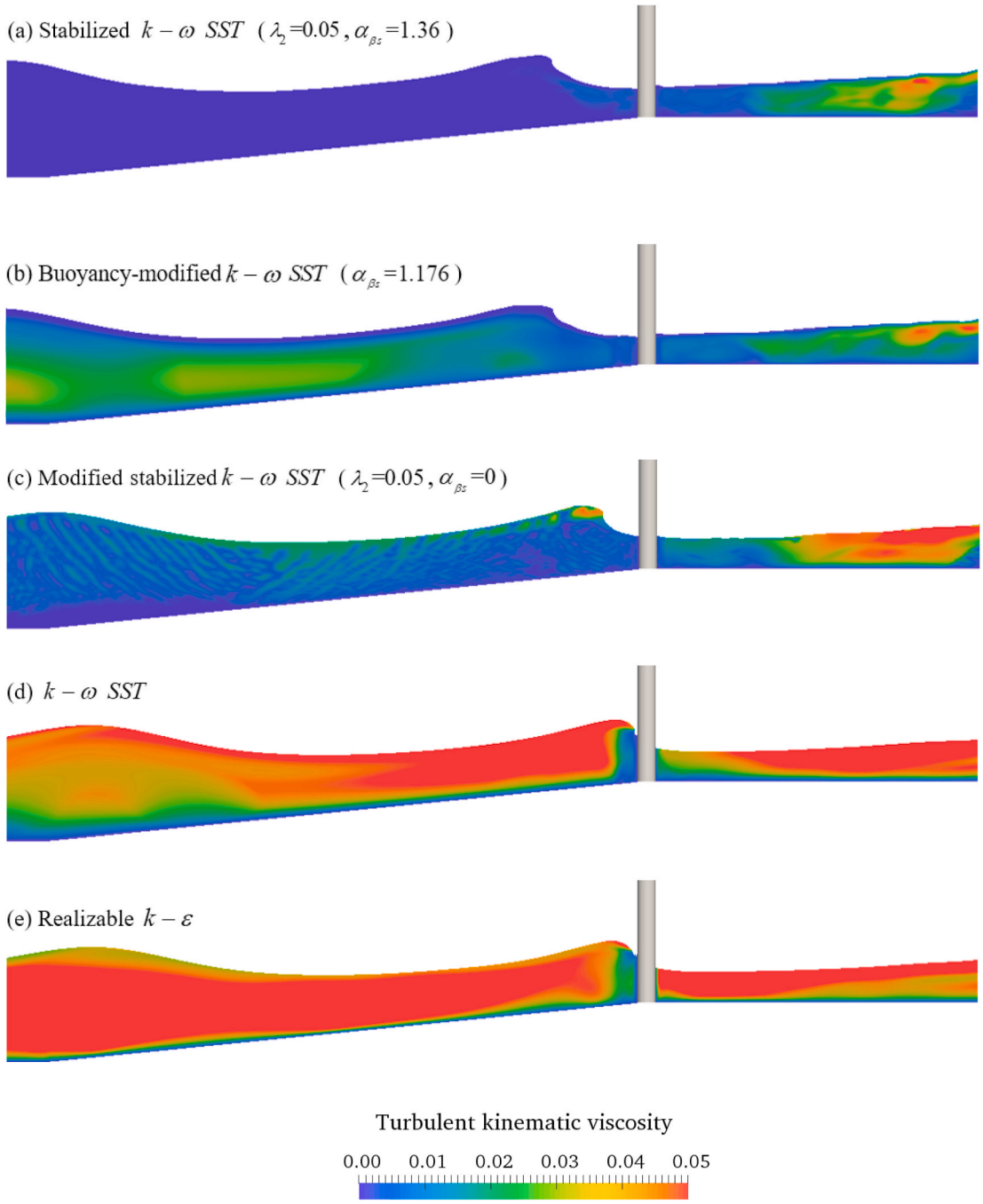

Fig. 12. Snapshots of the turbulent kinematic viscosity ν_t (m^2/s) at the breaking point with the (a) stabilized $k-\omega$ *SST* ($\lambda_2 = 0.05$, $\alpha_{\beta s} = 1.36$) (b) buoyancy-modified $k-\omega$ *SST* ($\alpha_{\beta s} = 1.176$) (c) modified stabilized $k-\omega$ *SST* ($\lambda_2 = 0.05$,$\alpha_{\beta s} = 0$) (d) $k-\omega$ *SST* (e) realizable $k-\varepsilon$.

lence models with the buoyancy modified term give more physical TKE, i.e., no turbulence before wave breaking and relatively large turbulence intensity in the post-breaking zone (behind the cylinder). However, the predicted breaking wave forces are smaller than that of the experimental data. This may be due to the properties of the VOF method. The VOF method usually results in a large air velocity at the free surface due to the continuity condition at the interface of water and air phases (Liu et al., 2020). This problem can be potentially improved by the large turbulence intensity produced by the $k-\omega$ *SST* turbulence model. Therefore, the $k-\omega$ *SST* turbulence model performs well on the surface elevation and the breaking wave force, despite overestimating levels of TKE. The realizable $k-\varepsilon$ turbulence model over-predicts the TKE and under-estimates the breaking wave force.

5. Conclusions and discussion

In this paper, different RANS turbulence models with the VOF method have been evaluated for investigating the interaction between the breaking waves and the vertical cylinder. The main conclusions in the present study can be drawn as follows:

(1) The position of the breaking point has a significant effect on the breaking wave force on the cylinder. The slight change in the wave front shape may lead to a large difference in the wave forces on the cylinder.
(2) The stabilized $k-\omega$ *SST* turbulence model ($\lambda_2 = 0.05$, $\alpha_{\beta s} = 1.36$) performs almost the same as no turbulence model for

predicting breaking wave forces. The wave breaks before hitting the vertical cylinder and the predicted breaking wave forces are smaller than the corresponding experimental data. The realizable $k-\varepsilon$ turbulence model under-predicts the surface elevation and the breaking wave force on the cylinder.

(3) The turbulence models with the buoyancy modified term (the stabilized $k-\omega$ *SST* ($\lambda_2 = 0.05$, $\alpha_{\beta s} = 1.36$) and the buoyancy-modified $k-\omega SST$ ($\alpha_{\beta s} = 1.176$)) significantly reduce the turbulent kinetic energy and turbulent kinematic viscosity in the flow field, showing more physical turbulence behavior before the wave breaking.

(4) The $k-\omega$ *SST* turbulence model accurately predicts the free surface elevations and the breaking wave forces as compared to the published experimental data. However, the level of the turbulent kinetic energy is overestimated, especially at the wave crest.

(5) The buoyancy modification coefficient mainly affects the flow characteristics at the free surface. While the stress limiter coefficient can affect the flow characteristics in the entire flow field.

It appears that none of the aforementioned turbulence models perform perfectly for predicting breaking waves past a vertical cylinder. The stabilized and buoyancy-modified $k-\omega$ *SST* models are more capable of turbulence intensity prediction. The combination of the VOF method and the $k-\omega$ *SST* turbulence model seems to give a reasonable prediction on the breaking point, which eventually predicts the wave forces well even though the turbulent kinetic energy is overestimated at the wave crest.

CRediT authorship contribution statement

Sen Qu: Conceptualization, Methodology, Software, Validation, Formal analysis, Investigation, Writing – original draft, Writing – review & editing, Visualization. **Shengnan Liu:** Conceptualization, Methodology, Software, Formal analysis, Investigation, Writing – review & editing, Supervision. **Muk Chen Ong:** Conceptualization, Investigation, Writing – review & editing, Resources, Supervision, Project administration, Funding acquisition.

Declaration of competing interest

The authors declare that they have no known competing financial interests or personal relationships that could have appeared to influence the work reported in this paper.

Acknowledgments

This study was supported in part with computational resources provided by the Norwegian Metacenter for Computational Science (NOTUR), under Project No: NN9372K.

References

Bihs, H., Kamath, A., Alagan Chella, M., Arntsen, Ø.A., 2016. Breaking-wave interaction with tandem cylinders under different impact scenarios. J. Waterw. Port, Coast. Ocean Eng. 142 (5), 04016005.

Bradford, S.F., 2000. Numerical simulation of surf zone dynamics. J. Waterw. Port, Coast. Ocean Eng. 126 (1), 1–13.

Brown, S., Greaves, D., Magar, V., Conley, D., 2016. Evaluation of turbulence closure models under spilling and plunging breakers in the surf zone. Coast Eng. 114, 177–193.

Chella, M.A., Bihs, H., Myrhaug, D., Muskulus, M., 2017. Breaking solitary waves and breaking wave forces on a vertically mounted slender cylinder over an impermeable sloping seabed. J.Ocean Eng.Marine Energy 3 (1), 1–19.

Choi, S.-J., Lee, K.-H., Gudmestad, O.T., 2015. The effect of dynamic amplification due to a structure's vibration on breaking wave impact. Ocean. Eng. 96, 8–20.

Chow, A.D., Rogers, B.D., Lind, S.J., Stansby, P.K., 2019. Numerical wave basin using incompressible smoothed particle hydrodynamics (ISPH) on a single GPU with vertical cylinder test cases. Comput. Fluids 179, 543–562.

Christensen, E.D., Bredmose, H., Hansen, E.A., 2005. Extreme wave forces and wave run-up on offshore wind turbine foundations. Proceedings of Copenhagen Offshore Wind 1–10.

Devolder, B., Troch, P., Rauwoens, P., 2018. Performance of a buoyancy-modified k-ω and k-ω SST turbulence model for simulating wave breaking under regular waves using OpenFOAM®. Coast Eng. 138, 49–65.

Hirt, C.W., Nichols, B.D., 1981. Volume of fluid (VOF) method for the dynamics of free boundaries. J. Comput. Phys. 39 (1), 201–225.

Irschik, K., Sparboom, U., Oumeraci, H., 2005. Breaking wave loads on a slender pile in shallow water, 2004 Coast Eng. 4, 568–580. World Scientific.

Jacobsen, N.G., Fuhrman, D.R., Fredsøe, J., 2012. A wave generation toolbox for the open-source CFD library: OpenFoam®. Int. J. Numer. Methods Fluid. 70 (9), 1073–1088.

Kamath, A., Chella, M.A., Bihs, H., Arntsen, O.A., 2016. Breaking wave interaction with a vertical cylinder and the effect of breaker location. Ocean. Eng. 128, 105–115.

Larsen, B.E., Fuhrman, D.R., 2018. On the over-production of turbulence beneath surface waves in Reynolds-averaged Navier–Stokes models. J. Fluid Mech. 853, 419–460.

Lin, P., Liu, P.L.-F., 1998. A numerical study of breaking waves in the surf zone. J. Fluid Mech. 359, 239–264.

Liu, S., Jose, J., Ong, M.C., Gudmestad, O.T., 2019. Characteristics of higher-harmonic breaking wave forces and secondary load cycles on a single vertical circular cylinder at different Froude numbers. Mar. Struct. 64, 54–77.

Liu, S., Ong, M.C., Obhrai, C., Gatin, I., Vukcevic, V., 2020. Influences of free surface jump conditions and different k - omega SST turbulence models on breaking wave modelling. Ocean. Eng. 217.

Mayer, S., Madsen, P.A., 2001. Simulation of breaking waves in the surf zone using a Navier-Stokes solver. Coast Eng. 928–941, 2000.

Menter, F.R., Kuntz, M., Langtry, R., 2003. Ten years of industrial experience with the SST turbulence model. Turbulence, heat and mass transfer 4 (1), 625–632.

Sawaragi, T., Nochino, M., 1984. Impact forces of nearly breaking waves on a vertical circular cylinder. Coastal Engineering in Japan 27 (1), 249–263.

Shih, T.-H., Liou, W.W., Shabbir, A., Yang, Z., Zhu, J., 1995. A new k-ε eddy viscosity model for high Reynolds number turbulent flows. Comput. Fluids 24 (3), 227–238.

Ting, F.C., Kirby, J.T., 1994. Observation of undertow and turbulence in a laboratory surf zone. Coast Eng. 24 (1–2), 51–80.

Wienke, J., Sparboom, U., Oumeraci, H., 2001. Breaking wave impact on a slender cylinder. Coast Eng. 1787–1798, 2000.

Xiao, H., Huang, W., 2014. Three-dimensional numerical modeling of solitary wave breaking and force on a cylinder pile in a coastal surf zone. J. Eng. Mech. 141 (8), A4014001.

Xie, Z., 2013. Two-phase flow modelling of spilling and plunging breaking waves. Appl. Math. Model. 37 (6), 3698–3713.